# Re-analysis of the Cassini RPWS/LP data in Titan's ionosphere. Part I: detection of several electron populations

**A. Chatain[1,2], J.-E. Wahlund[3], O. Shebanits[3,4], L. Z. Hadid[2,3], M. Morooka[3], N. J. T. Edberg[3], O. Guaitella[2], and N. Carrasco[1]**

[1] Université Paris-Saclay, UVSQ, CNRS, LATMOS, Guyancourt, France.

[2] LPP, Ecole polytechnique, Sorbonne Université, Institut Polytechnique de Paris, CNRS, Palaiseau, France.

[3] Swedish Institute of Space Physics, Uppsala, Sweden.

[4] Imperial College London, United-Kingdom.

Corresponding author: Audrey Chatain (audrey.chatain@ens-paris-saclay.fr)

**Key Points:**

- The Cassini Langmuir probe dataset in Titan's ionosphere is re-analyzed with a specific interest on the electron density and temperature.
- 2 to 4 cold electron populations with distinct potentials are observed.
- Electron populations vary with altitude and solar illumination suggesting origins linked to solar photons, magnetospheric particles and dust

## Abstract

Current models of Titan's ionosphere have difficulties in explaining the observed electron density and/or temperature. In order to get new insights, we re-analyzed the data taken in the ionosphere of Titan by the Cassini Langmuir probe (LP), part of the Radio and Plasma Wave Science (RPWS) instrument. This is the first of two papers that present the new analysis method (current paper) and statistics on the whole dataset. We suggest that between 2 and 4 electron populations are necessary to fit the data. Each population is defined by a potential, an electron density and an electron temperature and is easily visualized by a dinstinct peak in the second derivative of the electron current, which is physically related to the electron energy distribution function (Druyvesteyn method). The detected populations vary with solar illumination and altitude. We suggest that the 4 electron populations are due to photo-ionization, magnetospheric particles, dusty plasma and electron emission from the probe boom, respectively.


## 1 Introduction

The Cassini mission explored the Saturnian system from 2004 to 2017 and gave us unprecedented insights on the ionosphere of Titan, the biggest moon of Saturn (Coates et al., 2007; Wahlund et al., 2005; Waite et al., 2005). This ionized environment hosts a complex ion chemistry that leads to the formation of organic aerosols (Vuitton et al., 2019; Waite et al., 2007). The Cassini mission investigated Titan at the occasion of 126 close flybys, and probed the ionosphere below the altitude of 1200 km for 57 of these flybys. There is a substantial coverage of measurements taken at different solar zenith angles, latitudes and seasons, enabling statistical analyses.

The study here is focused on electrons in Titan's ionosphere. The electron density was previously observed to be mainly governed by solar photons during the day (Ågren et al., 2009). Photoionization of the neutral molecules lead to a maximum electron density (~2000 $cm^{-3}$) around 1100 km altitude. The electron density have also been observed to vary (up to factor 2 at the peak) with the solar cycle (Edberg et al., 2013). On the nightside, electron transport from the dayside and the thermalization of magnetospheric electrons give a constant electron density of ~400-700 $cm^{-3}$ from 1200 km to < 950 km (Ågren et al., 2009; Cravens et al., 2009; Cui et al., 2009; Shebanits et al., 2017b).

Below 1100 km of altitude, positive, negative ions and dust have increasing densities, and start to affect the electrons (Shebanits et al., 2013, 2016; Waite et al., 2007). In particular, dust particles in a dense ionized environment tend to attract electrons and charge negatively (e.g. Farrell et al., 2009; Shukla & Mamun, 2015). It explains whay the electron density decreases below 1100 km, while the density of ions and negatively charged dust increase and become the dominant negative charge carriers (e.g. Shebanits et al., 2013, 2016).

The temperature of the bulk electrons can be deduced from measurements by the Langmuir probe on-board Cassini. Ågren et al. (2009) and Edberg et al. (2010) derived the electron temperature profiles (assuming a single Maxwellian electron distribution) from 52 flybys down to ~900 km of altitude and stated a rather stabilized temperature below 1100 km. The observed values ranged from 0.03 to 0.06 eV (≈ 350-700 K).

Several models have been developed to understand the processes at work in Titan's ionosphere (e.g. Galand et al., 2014 and references therein). Nevertheless, model results either predict too cold

electrons (< 0.02 eV; < 200 K) at 900 km (Mukundan & Bhardwaj, 2018; Richard et al., 2011) or an overestimated electron density by a factor of 2 (Vigren et al., 2013, 2016). The addition of the negative ions to a photoionisatoin model has been shown to decrease the discrepancy with the measurements (Shebanits et al., 2017a).

The present work aims to closely investigate the measurements of the electron density and temperature in the ionosphere of Titan, focusing on the interaction between electrons and negative ions and dust. For this purpose, we re-analyzed the measurements acquired by the Langmuir probe (LP) part of the Radio and Plasma Wave Science (RPWS) investigation on-board Cassini, during the 13 years of the mission. This work is presented in two parts. In a first paper (this one), we detail the method used for the re-analysis of the data and the detection of several electron populations. A second paper (Chatain et al., n.d.), referred as 'paper II', presents the results obtained for 57 flybys and discusses the origins of the detected electron populations.

## 2 Methods

### 2.1 Langmuir Probe measurements

The Langmuir probe on-board Cassini was built by the Swedish Institute of Space Physics (IRF). It was positioned below the radio antenna, on a 1.5 m boom to minimize electric perturbation from the spacecraft (Gurnett et al., 2004). The probe was a sphere of titanium of 5 cm in diameter, coated with titanium nitride, chosen foremost for its electrical work function stability, chemical inertness, high reflectivity and limited photoelectric effects. It is also very hard, enhancing solid particle impact resistance and eliminating hysteresis effects that are observed with other surface coatings (Wahlström et al., 1992). A small part of the stick (the stub) closest to the sphere was kept at the probe potential to ensure a symmetric potential pattern and sampling around a swept probe. A cleaning mode enabled to remove a possible contamination on the surface. In this mode, the potential of the sphere was set at +32 V to induce sputtering of the probe with high energy electrons.

In this study, we used the measurements from the sweep mode of the probe. The current collected by the probe during the voltage sweep enables to deduce the electron density and temperature (among other useful derived parameters of interest). On Titan, the probe usually acquired double-sweeps, in 512 x2 voltage steps, from +4 V to -4 V, and back to +4 V, to give an idea of possible surface contamination effects. In addition, to detect any charging effects, for both of the sweeps the current was measured twice at each voltage step.

In this work, we first investigated the reproducibility of the measurements with the two voltage sweeps (named 'down' and 'up'), and the double measurements at each voltage step (resp. 'down1'-'down2' and 'up1'-'up2'). We observed that 'down1' and 'down2' are always very close to each other: the current stabilizes quickly after each voltage step. However, during the increasing voltage phase ('up1'and 'up2'), the current continues to increase sligthly between the two measurements. Further details are given in Appendix A.

In the following, we did not take the average of 'down' and 'up' because in some cases a shift in the measured plasma potential between both would distort the average signal. We generally used the average of the decreasing part of the sweep ('down'). Nevertheless, we used also the average of 'up1' and 'up2' in the few cases where the decreasing part of the sweep was not acquired. We

analyzed the impact of using the 'down' or the 'up' signal in our study and concluded that this effect was negligible compared to the fit error bars (see further). An example is given in Supporting Information Figure S1.

### 2.2 Theory to fit the electron and positive ion current

The Orbital Motion Limited (OML) theory is used to fit the voltage sweeps measured by the Langmuir probe. A correction is added in the attractive bias voltage region using the Sheath Limited theory (SL).

The OML theory, first described by Mott-Smith & Langmuir (1926), deduces information on the charged particles from the current measured by the probe, based on the conservation of energy and angular momentum. No particle is assumed to come from the probe itself and the bulk particle speed distribution is assumed Maxwellian. The OML theory is valid when the probe radius is smaller than the Debye length in the probed region. In these conditions, the electron and ion currents (respectively $I_e$ and $I_i$) are described by two different equations depending on the sign of $\Delta U = U_{bias} - U_P$ (Wahlund et al., 2009; Whipple, 1965), $U_{bias}$ being the potential of the probe and $U_P$ the characteristic potential of the electron/ion population in the plasma. The electron current $I_e$ (resp. the ion current $I_i$) is expressed as a function of $I_{e,0}$ (or $I_{i,0}$) and $\chi_e$ (resp. $\chi_i$):

$$I_x = I_{x,0}\,(1 - \chi_x) \qquad x = e \text{ if } \Delta U > 0,\ x = i \text{ if } \Delta U < 0 \text{ ['attractive' part for electrons]} \tag{1}$$

$$I_x = I_{x,0}\exp(-\chi_x) \qquad x = e \text{ if } \Delta U < 0,\ x = i \text{ if } \Delta U > 0 \text{ ['repelling' part for electrons]} \tag{2}$$

The two equations join in $\Delta U = 0$. Then, the collected current $I_{x,0}$ is formulated as follows. It combines the effect of flow kinetic energy and thermal energy (Fahleson et al., 1974):

$$I_{x,0} = -A_{LP}.n_x.q_x.\sqrt{\frac{v_x^2}{16} + \frac{k_B T_x}{2\pi.m_x}} \tag{3}$$

$A_{LP}$ is the surface area of the probe. $n_x$, $q_x$, $v_x$, $T_x$ and $m_x$ are respectively the density, charge, velocity, temperature and mass of electrons or ions, and $k_B$ is the Boltzmann constant.

The parameter $\chi_x$ depends on $\Delta U$ and is expressed as:

$$\chi_x = \frac{q_x.\Delta U}{\frac{m_x v_x^2}{2} + k_B T_x} \tag{4}$$

In the case of electrons, the flow kinetic energy term can be neglected compared to the thermal term. It is the opposite in the case of ions (positive and negative), which are heavier than electrons and transported along the ion ram flux. When $\Delta U \ll 0$, the collected current is governed by positive ions while it is dominated by electrons when $\Delta U > 0$.

In Titan's ionosphere, the Debye length ($\lambda_D \approx 2.5 - 10.5\ cm$) is similar to the radius of the probe ($r_p = 2.5\ cm$). It is the limit of validity to use the OML theory. Therefore, a small correction is added by using the Sheath Limited (SL) theory (Bettinger & Walker, 1965; Whipple, 1965), valid in a collisionless maxwellian plasma. It adds the dependence of the sheath thickness ($s$) with the potential and size of the probe and changes the expression of the attractive part. For electrons, it gives for $\Delta U > 0$:

$$I_e = I_{e,0} \times \left[1 + \xi \times \left(1 - \exp\left(-\frac{\chi_e}{\xi}\right)\right)\right]$$
$$with \quad \xi = \left(\frac{s}{\rho} + 1\right)^2 - 1, \qquad \rho = \frac{r_p}{\lambda_D} \qquad (5)$$
$$and \quad s = 0.83.\sqrt{\chi_e}.\rho^{\frac{1}{3}}$$

The expression of the sheath thickness ($s$) is empirically obtained by Bettinger and Walker (1965) in the case of spherical bodies. These expressions converge to the OML expressions when $s \gg r_p$.

The electron temperature and the Electron Energy Distribution Function (EEDF) can be obtained from the 'transition region', the part of the voltage sweep where the electron current starts to dominate the positive ion current, i.e. for $\Delta U$ being slightly negative (of a few tenths of volts in the conditions of Titan's ionosphere).

In this transition region, the positive ion current is not always negligible compared to the electron current. To obtain the electron current, the measured (total) current is therefore corrected from the positive ion part, fitted by a linear curve (see Equation (1)). An example is given in Supporting Information Figure S2.

### 2.3 Example of electron current collected in Titan's ionosphere: observation of several electron populations

The electron part is fitted with Equations (2) and (5). Nevertheless, using only one electron 'population' (i.e. one combination of Equations (2) and (5)) results in a poor fit of the electron current collected in the ionosphere. Generally, a second population has to be added. It leads to two different sets of ($U_P$, $n_e$, $T_e$). An example is shown in Figure 1.

Below 1300 km, two maxwellian populations of electrons are often still not sufficient to correctly fit the electron current. A third, and in rare occasions a fourth, population is required. An example with three populations is shown in Figure 2 and examples with one and four populations are given in Supporting Information Figure S3 and S4. In conclusion, the analysis of voltage sweeps in the ionosphere of Titan often leads to 2-4 sets of ($U_P$, $n_e$, $T_e$) per sweep. The fitting procedure is detailed in Appendix B.

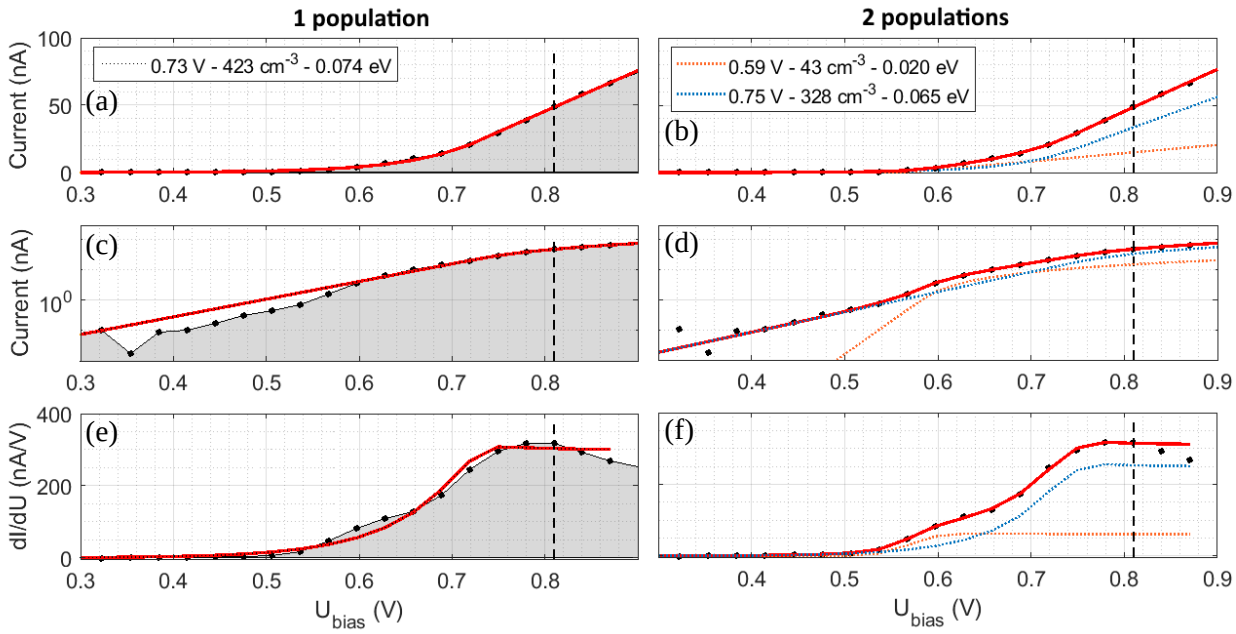


**Figure 1**. Fitting of the voltage sweep acquired during T50 at 1241 km altitude. (a,c,e) One electron population is used for fitting. (b,d,f) Two electron populations are used for fitting. The fit results $(U_p, n_e, T_e)$ for each population are indicated on the graphs. The part of the curves after the dashed line corresponds to a part possibly distorted by the effect of a logarithmic pre-amplifier, and should not be used without further consideration.

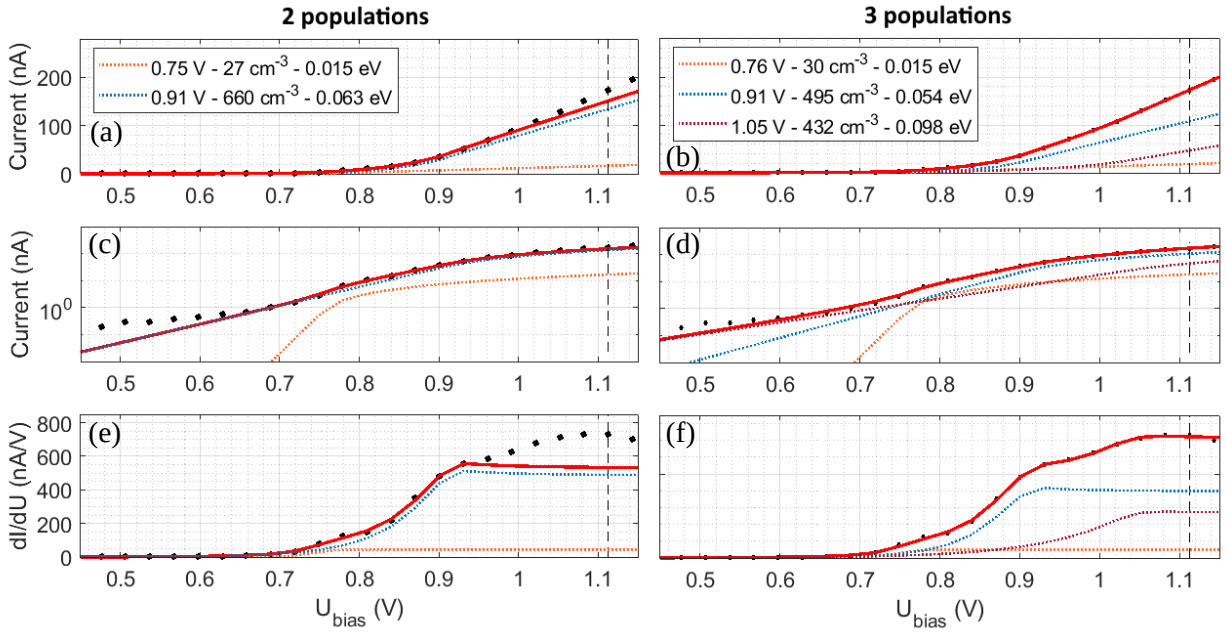


**Figure 2**. Fitting of the voltage sweep acquired during T50 at 1125 km altitude. (a,c,e) Two electron populations are used for fitting. (b,d,f) Three electron populations are used for fitting. The fit results $(U_p, n_e, T_e)$ for each population are indicated on the graphs. The part of the curves after the dashed line corresponds to a part possibly distorted by the effect of a logarithmic pre-amplifier, and should not be used without further consideration.

176

177 2.4 The second derivative of the electron current ($d^2I/dU^2$): an effective method to detect
178 the electron populations

179 The second derivative of the current is a good indicator of the presence of several electron
180 populations. Each peak corresponds to a population, and its area is globally proportional to the
181 electron density associated (this is explained in Section 2.5). Figure 3 shows $d^2I/dU^2$ associated
182 with the fitted sweeps plotted in Figure 1 and 2. Cases with 1 and 4 populations are shown in
183 Supporting Information Figure S5.

184 The data points are at very low resolution, with only four to ten points per peak. Consequently, the
185 computation of the second derivative is strongly impacted. This effect is illustrated in Figure 3:
186 the red curve shows $d^2I/dU^2$ computed from the fit with the (low) resolution of the data points, and
187 the orange dotted-dashed line gives $d^2I/dU^2$ with a high resolution (with >200 points per peak).

188 The confidence intervals on the fit results ($U_P$, $n_e$, $T_e$) for all the populations are also computed
189 (see details in Appendix C) and are plotted in the Figures of section 3.2. The uncertainty is larger
190 in the cases with more electron populations, in particular when their parameters $U_P$ are close.

191

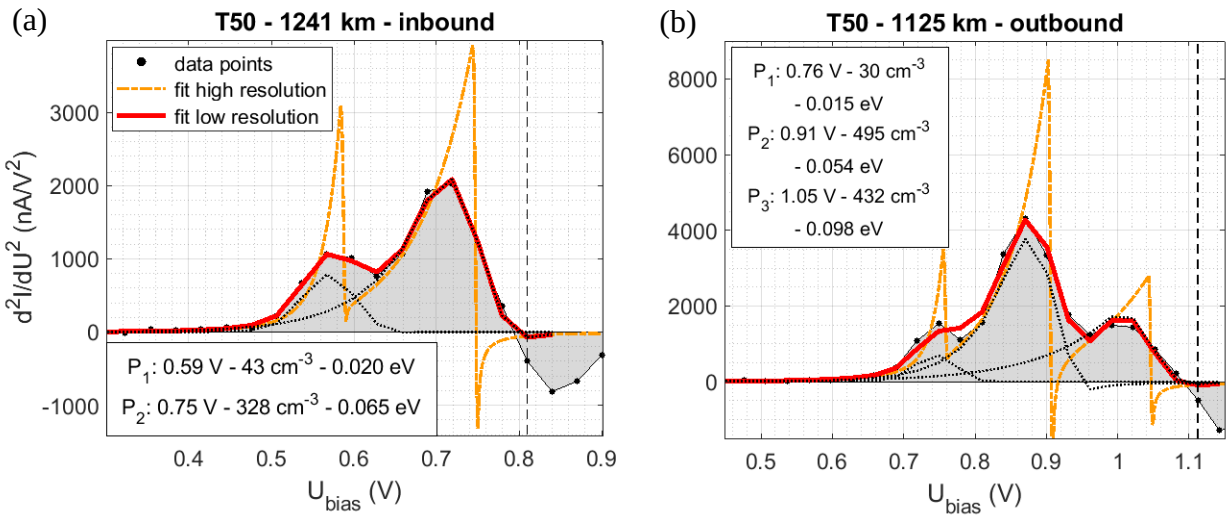


192

193 **Figure 3.** Second derivative of current for the sweeps shown in (a) Figures 1 and (b) Figure 2. The fitted
194 curves shown in Figures 1 and 2 are derived to obtain $d^2I/dU^2$, at the resolution of the data points (red line)
195 and at higher resolution (orange dotted-dashed line). The fit results ($U_p, n_e, T_e$) for each population are
196 indicated on the graphs. The part of the curves after the dashed line corresponds to a part possibly distorted
197 by the effect of a logarithmic pre-amplifier, and should not be used without further consideration.

198

199

200 2.5 Link between the second derivative of the electron current and the Electron Energy
201 Distribution Function (EEDF)

202 This section explains the link between the second derivative of the current ($d^2I/dU^2$) and the
203 Electron Energy Distribution Function (EEDF). It aims to justify the attribution of electrons
204 populations to peaks in the second derivative. The presented method finally gives the Maxwellian
205 EEDF of each of the electron populations detected on a same measurement.

206

207 *2.5.1 The Druyvesteyn method*

208 The Druyvesteyn method (Druyvesteyn, 1930; Lieberman & Lichtenberg, 2005) was used to
209 compute the EEDF from the electron current measured by the Langmuir probe. The method is
210 valid for any convex probe geometry and does not depend on the probe dimension compared to
211 Debye length, or on the ratio $T_i/T_e$. The EEDF is computed from the second derivative of the
212 current, and the electron density is equal to the integral of the EEDF (see details in Appendix D):

$$EEDF_{Dr}(\Delta U) = \frac{2\sqrt{2}}{A_{LP}\, e^2}\sqrt{\frac{m_e\,.(-\Delta U)}{e}}\,\frac{d^2 i}{d\Delta U^2} \qquad [J^{-1}.m^{-3}]$$
$$with\ n_e = \int_0^{+\infty} EEDF_{Dr}\big(E(\Delta U)\big)\,.dE \quad and \quad E(\Delta U) = -e.\Delta U \tag{6}$$

213 If the Druyvesteyn method is applied to the expression of the current given in Equation (2), it gives
214 back the expression of an EEDF for a Maxwellian speed distribution:

$$EEDF_{Maxw}(E) = \frac{2}{\sqrt{\pi}}.(k_B.T_e)^{-\frac{3}{2}}.n_e.\sqrt{E}.\exp\left(-\frac{E}{k_B.T_e}\right) \tag{7}$$

215

216 *2.5.2 EEDF: example with one population*

217 This section presents a simple case with one electron population (introduced in Figure S3 and
218 S5(a)). Figure 4 compares the EEDF obtained by applying the Druyvesteyn method to the data
219 points (Equation (6)), to the 'Maxwellian' EEDF computed with the fitted electron density and
220 temperature (Equation (7)). They do not perfectly match (the maximum of the peak is shifted)
221 because of the low resolution of the data points. Indeed, the Druyvesteyn method uses the second
222 derivative of the current, which is highly distorted because of the low number of data points (e.g.
223 the sharp initial increase is lowered by this effect).

224 To show this effect, the Druyvesteyn method is applied to the fit of the current. The EEDF obtained
225 using a fitting curve at high resolution (> 200 points per peak) superimposes very well with the
226 'Maxwellian' EEDF. On the other side, the EEDF obtained using a fitting curve with the resolution
227 of the Langmuir probe data points (4-10 points per peak) matches well with the EEDF obtained
228 from the data points. The EEDF obtained using the Druyvesteyn method on the Langmuir probe
229 data points is therefore fairly well represented by a 'Maxwellian' EEDF if one takes the problem
230 of low resolution into account.

231

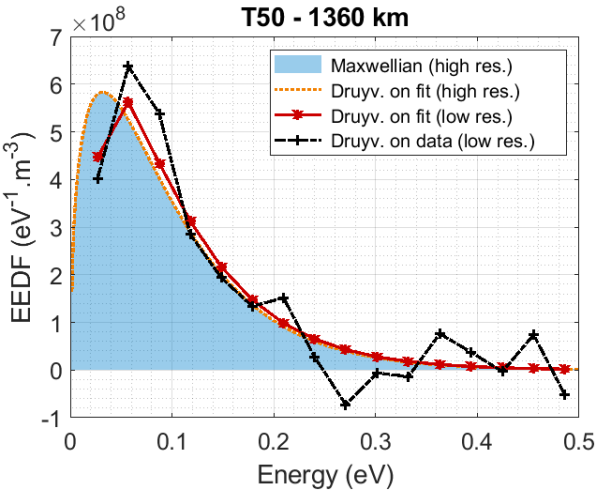


**Figure 4.** Example of EEDF obtained from Langmuir probe data with only one population using the Druyvesteyn method (dotted-dashed black line). Comparison to the EEDF obtained with the Druyvesteyn method applied to the fit at low resolution (red line), at high resolution (orange dotted line), and to the 'Maxwellian' EEDF from fitted $n_e$ and $T_e$ (blue area).

### *2.5.3 EEDF: example with several populations*

In the case of data showing several populations, applying the Druyvesteyn method is less straightforward: the method requires one 'plasma potential' $U_P$, whereas the fit gives as much $U_P$ as populations detected. Figure 5 shows the case of two populations. The Druyvesteyn method is applied to the data points using the $U_P$ potential from (a) the first population and (b) the second population. In Figure 5b, the two population peaks appear in reverse order compared to the plot of $d^2I/dU^2$ in Figure 3a, because the x-axis is reversed ($E = -e\,.\,\Delta U \;\propto -\mathrm{U_{bias}} + U_P$).

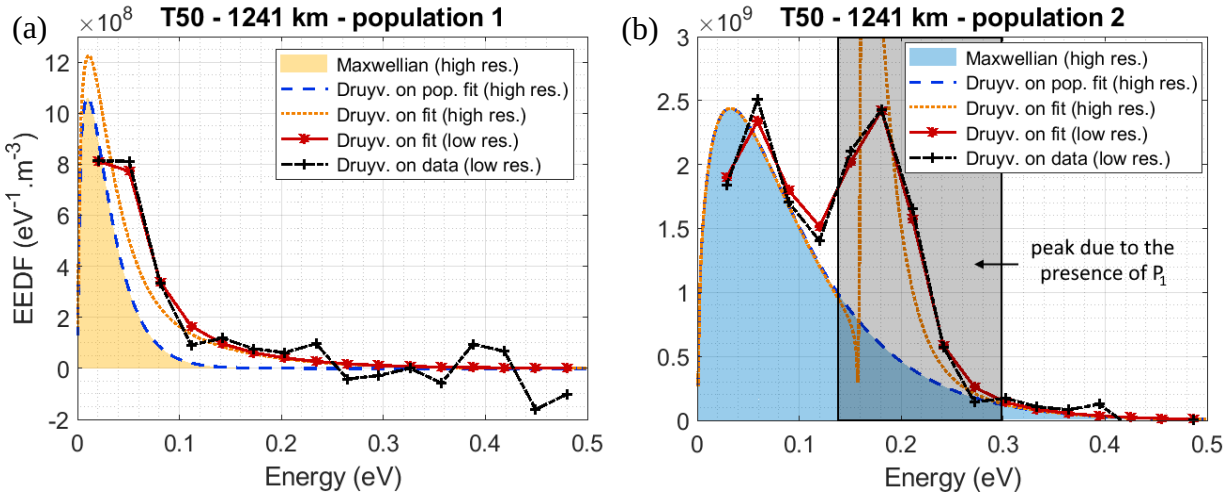


**Figure 5.** Example of EEDF obtained from Langmuir probe data with two populations using the Druyvesteyn method: (a) for population 1; (b) for population 2. Comparison of the EEDF using the Druyvesteyn method on data points (dotted-dashed black line) to the EEDF obtained with the Druyvesteyn method applied to the fit at low resolution (red line), at high resolution (orange dotted line), to the fit of

only one population at high resolution (dashed blue line) and to the 'Maxwellian' EEDF from fitted $n_e$ and $T_e$ (area).

Figure 5 shows that in the case of several electron populations, the EEDF computed for one population with the Druyvesteyn method is disturbed by the other populations with close values of $U_P$. To observe this effect, the Druyvesteyn method is applied to the fit of the data points with the two populations (orange line), and to the fitted current corresponding only to one population (dashed blue line). Therefore, if one takes into account both the presence of nearby populations (supplementary peak at higher energy) and the effects of low resolution (shift of the main peak), the EEDF from data points can reasonably be modelled by a 'Maxwellian' EEDF (shaded area). An example with 3 populations is given in Supporting Information Figure S6.

### *2.5.4 Diversity of EEDF combinations for the different populations*

The 'Maxwellian' EEDF of the electron populations are compared in Figure 6. As mentioned in Section 2.5.1, the area under each EEDF corresponds to the electron density of each population and the position of the maximum of the EEDF is related to the electron temperature.

Figure 6 shows the variability of the electron distribution (i.e. the changes in electron populations) for different flybys. It illustrates three very different cases obtained at ~1000 km altitude, which are representative of the three flyby groups (G1, G2 and G3) presented in details below, in Section 3.1.

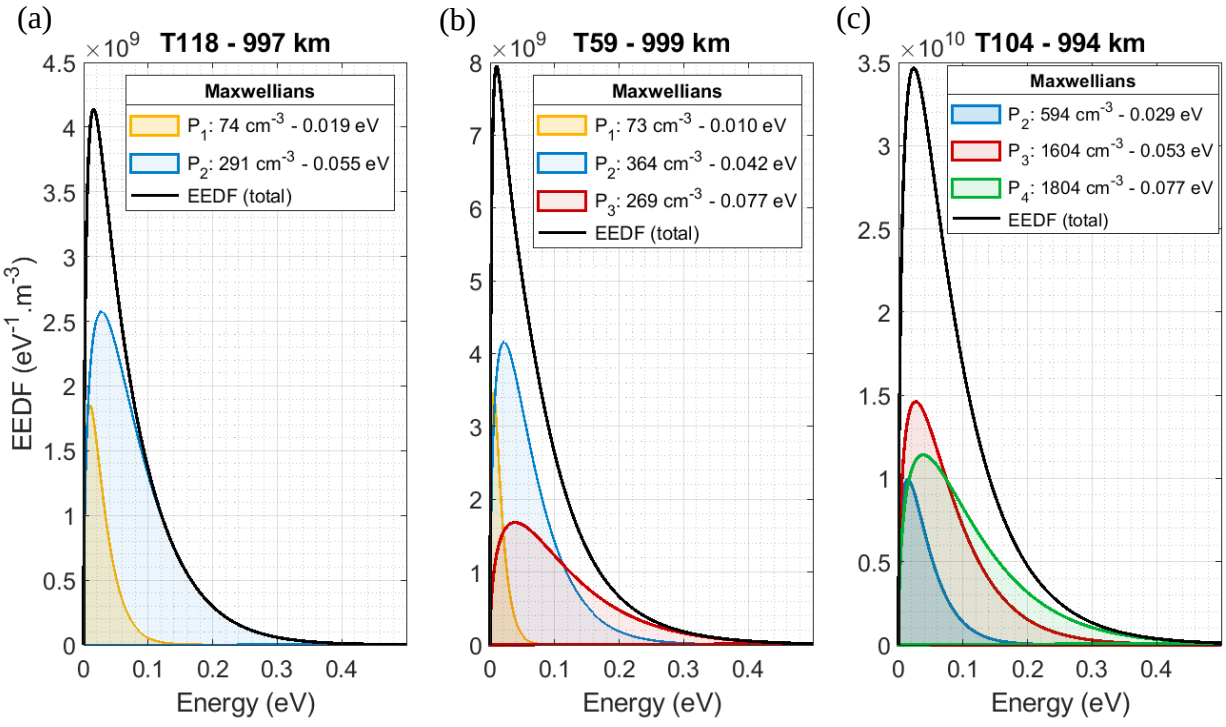


**Figure 6.** EEDF obtained from Maxwellian populations, at ~1000 km altitude for the flybys: (a) T118 (group G1); (b) T59 (G2); (c) T104 (G3).

The first case (from the group G1) shows two populations (named $P_1$ and $P_2$). The area (and so the electron density) of $P_2$ dominates $P_1$. The second case (G2) has one additional population ($P_3$). The area of $P_2$ and $P_3$ are equivalent and higher than the area of $P_1$. We observe that $P_3$ distribution is in average at higher energy than the distribution of $P_2$: its electron temperature is higher. Finally, the group G3 shows still another population ($P_4$) and $P_1$ becomes negligible compared to the others. $P_3$ dominates $P_2$ in density. $P_4$ characteristics vary with altitude: it can be denser than the others, and it is usually hotter.

## 3 Results and discussions

### 3.1 Variation of the electron populations with altitude and Solar Zenith Angle (SZA)

#### *3.1.1 Variation with altitude*

Voltage sweeps evolve during a flyby. The number of observed peaks in the second derivative of the current ($d^2I/dU^2$) varies with altitude. Therefore, the number of electron populations (and consequently the electron distribution) changes with altitude for a given flyby. We focus on the part of the ionosphere below 1200 km. The Langmuir probe took measurements at these altitudes at the occasion of 57 flybys.

The curves of $d^2I/dU^2$ as a function of the altitude obtained from the 57 flybys allow to easily classify Titan flybys in three groups. Each group has a different number of electron populations, with different characteristics. They are described in Table 1 and examples of profiles for the three cases are shown in Figure 7. All the profiles have similar $d^2I/dU^2$ curves around 1250-1200 km, showing usually three peaks. However, this curve evolves differently with altitude in the three cases. At lower altitude, in all cases, there is a main hump formed either by one large peak, two or three peaks (further named $P_1$, $P_2$, $P_3$ for clarity). In addition, for the profiles of the group G3, a small hump detached from the main one ($P_4$), at higher voltage, is observed below ~1200 – 1150 km altitude.

**Table 1.** Definition of the 3 flyby groups and their corresponding flybys. The flybys studied in details in Figure 7 and Scetion 3.2 are indicated in bold.

| Name of the flyby group | Characteristics of $d^2I/dU^2$ at lower altitude | Flybys (T#) |
|---|---|---|
| G1 | 2 separated peaks | 21, 25-28, 55, **118**-119 |
| G2 | 3 peaks | 5, 16, 46, 50, 56-**59**, 65, 117, 121 |
| G3 | 1 large peak (or 2 close) + 1 further, at higher $U_{bias}$ | 17, 20, 23, 39-43, 47-48, 51, 83-88, 91-92, 95, 100, **104**, 106-108, 113, 126 |
| G1/G2 | with different characteristics on inbound and outbound | 29-30, 32, 120 |
| G2/G3 | | 18-19, 36, 49, 61, 70-71 |

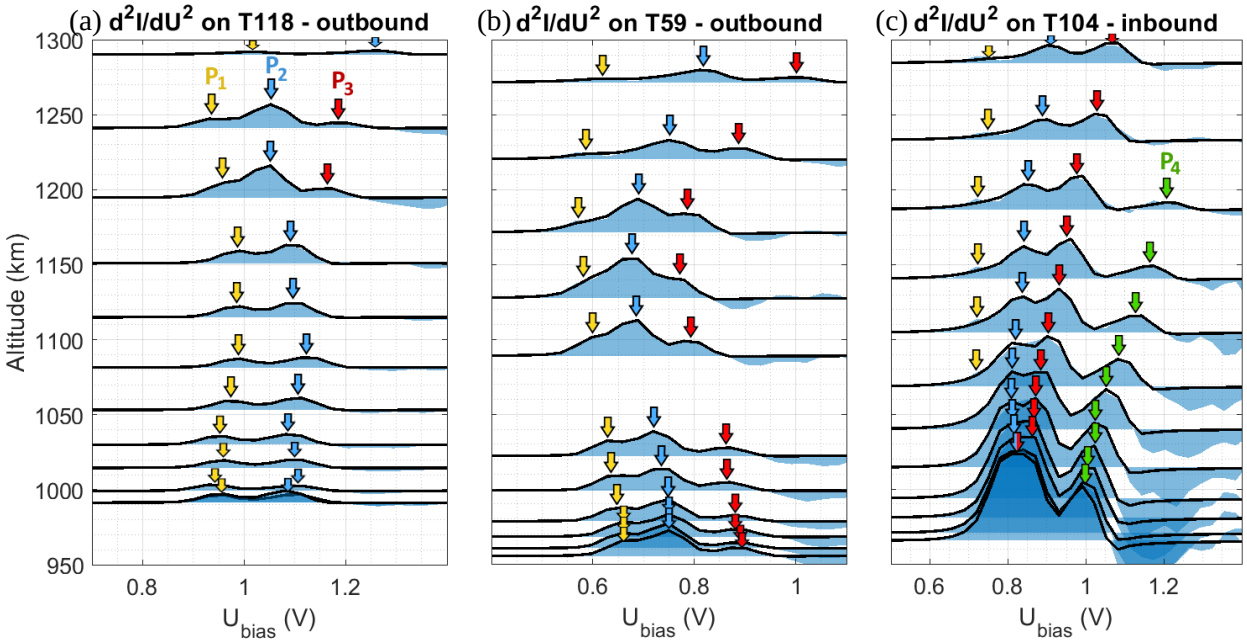


**Figure 7**. Examples of $d^2I/dU^2$ profiles with altitude: (a) T118 (from G1), (b) T59 (G2) and (c) T104 (G3). The second derivative of the electron current from Langmuir probe data (blue area) is superimposed to $d^2I/dU^2$ from the fit (black line). The scaling of $d^2I/dU^2$ is the same for all the plots. Arrows indiquate the peaks corresponding to the 4 populations.

### *3.1.2 Variation with Solar Zenith Angle (SZA)*

The detection of populations $P_3$ and $P_4$ are strongly dependent on the Solar Zenith Angle (SZA). Figure 8 shows the repartition of the electron populations with altitude and SZA in the case of 57 Cassini flybys. The population $P_4$ appears always below ~1200 km and at SZA < 80-90° (such flybys belong to the group G3), and the cases without a $P_3$ population at lower altitude (group G1), are observed only on the nightside, at high SZA (>~120°).

The distribution of the 57 flybys in three groups is then closely correlated to their SZA. The group G1 corresponds to flybys on the far nightside (SZA >~120°), G2 to flybys on nightside close to the terminator, and G3 to dayside (SZA < 80-90°).

In conclusion, the variation with altitude and SZA of the detected peaks of $d^2I/dU^2$ can be schematized as in Figure 9. Each peak is attributed to an electron population among $P_1$, $P_2$, $P_3$ and $P_4$. At ~1200-1300 km, $d^2I/dU^2$ graphs are very similar at all SZA, with three populations ($P_1$, $P_2$, $P_3$). Below 1200 km, $d^2I/dU^2$ varies differently depending on SZA: (G1) on the far nightside (SZA >~120°), $P_3$ disappears; (G2) close to the terminator, the three populations are kept at lower altitudes, with an increase of the area of the $P_2$ peak; (G3) and on dayside, $P_2$ and $P_3$ grow, $P_1$ becomes negligible and $P_4$ appears. In some occasions, $P_2$ and $P_3$ peaks merge.

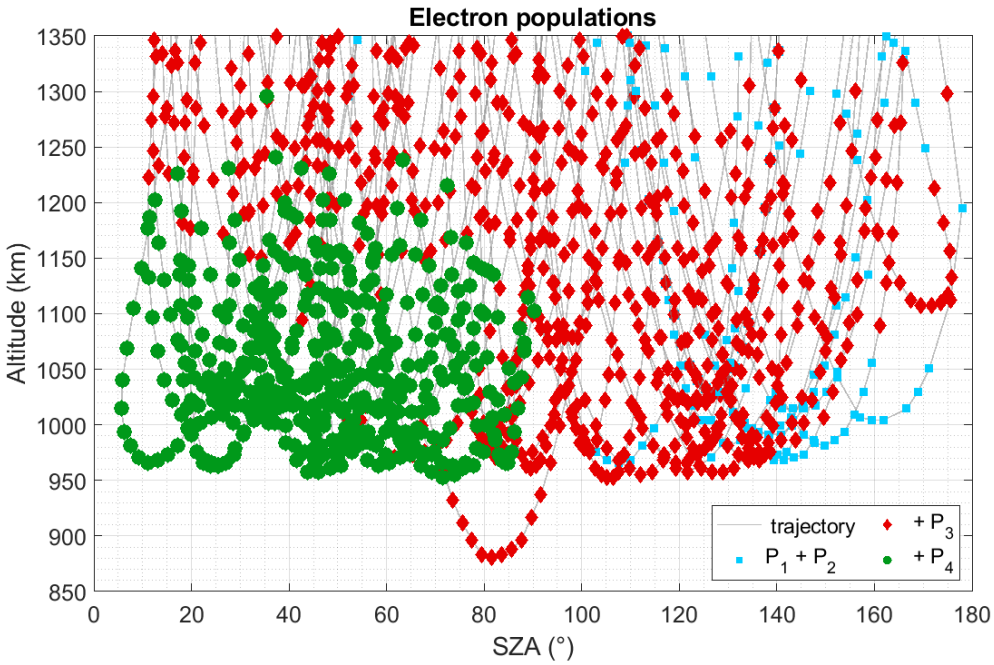


**Figure 8.** Detection of electron populations as a function of altitude and SZA, from 57 flybys. Blue squares represent sweeps with only populations $P_1$ and $P_2$, red diamonds show the presence of $P_3$, and green dots are for $P_4$.

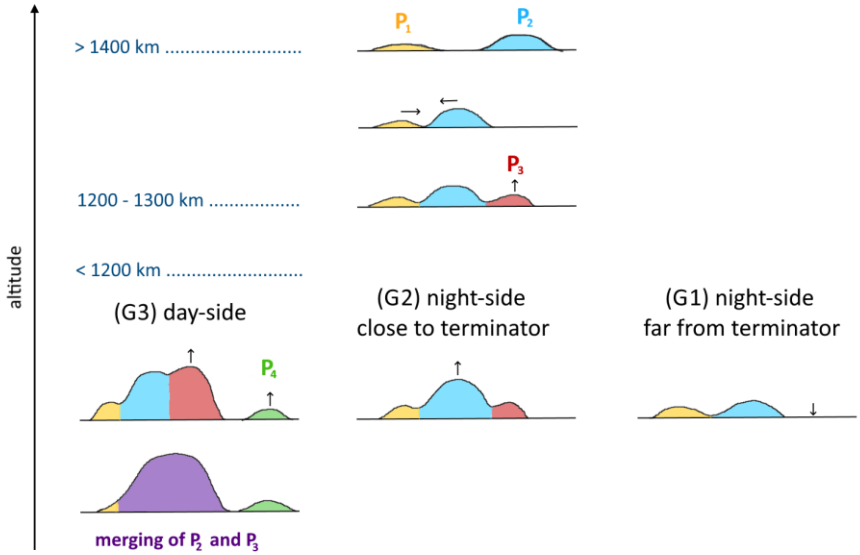


**Figure 9.** Summary scheme of the evolution of $d^2I/dU^2$ peaks with altitude in the 3 cases: nightside far from terminator (G1), nightside close to terminator (G2) and dayside (G3). Small arrows indicate the evolution trends with decreasing altitude.

## 3.2 Electron densities and temperatures

The results on electron density and temperature are discussed separately for each of the 3 groups (G1, G2 and G3), in the following sub-sections (respectively 3.2.1, 3.2.2 and 3.2.3).

### *3.2.1 Nightside far from the terminator (group G1)*

#### *3.2.1.1 Typical altitude profiles*

Figure 10 shows inbound (solid lines) and outbound (dashed lines) profiles of the electron density and temperature typical of the far nightside (G1). The confidence interval at 95% is indicated with shaded areas (see computation in Appendix C). The dominant population observed is $P_2$ (blue), with a rather constant temperature around 40-60 meV (460-700 K) below 1150-1250 km altitude. The density of this population peaks at an altitude varying between 1150 and 1250 km altitude. The population with the lowest $U_p$ ($P_1$, orange) is very constant with altitude. Its density is low, less than 100 $cm^{-3}$. Its temperature is around 10-20 meV (120-230 K), at the detection limit of the probe. In addition, a third population appears ($P_3$, red) at the ionospheric peak, when the total electron density exceeds 500 $cm^{-3}$. It has a temperature higher than the other populations, around 60-90 meV (700-1040 K).

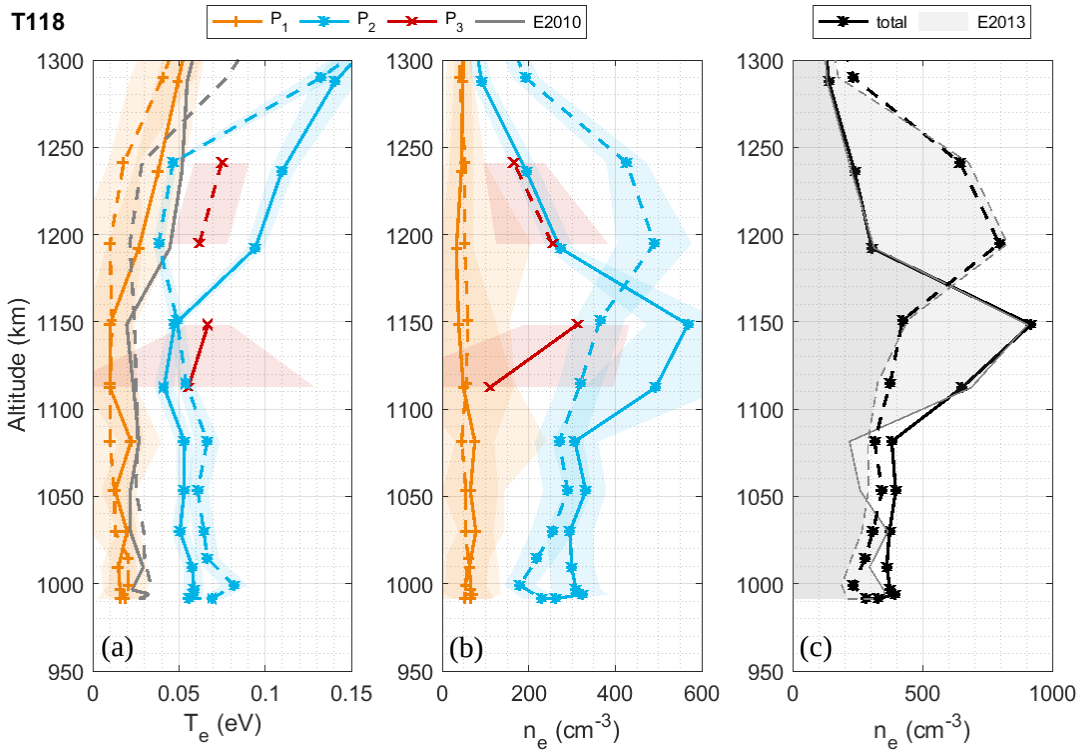


**Figure 10.** Electron temperature (a) and density (b,c) profiles in the case of T118, an example of a G1 group flyby (far nightside); inbound (line) and outbound (dashed line); results for the different populations $P_1$, $P_2$ and $P_3$ (colors). The fit confidence intervals at 95% are indicated in colored shaded area. The total density (sum of the densities of all the populations) is indicated in black. Comparison to Edberg et al. (2013, 2010), respectively noted E2013 and E2010 (grey).

The total electron density obtained is consistent with previous measurements acquired with different methods (Ågren et al., 2009; Edberg et al., 2013; Garnier et al., 2009). The comparison of our fit to the density measurements by Edberg et al. (2013) serves as a validation tool. As for electron temperature, results are compared to a previous analysis (Edberg et al., 2010). This previous analysis usually gives an electron temperature between the ones found for $P_1$ and $P_2$, and therefore sometimes colder than the dominant population ($P_2$) temperature. For instance, in the case of T118 shown in Figure 10, they obtained a temperature not representative of the main population of electrons ($P_2$). It shows that using several electron populations in the fitting of the sweeps significantly improves the analysis, since it attributes a temperature for each population, and consequently, the temperature of the dominant electron population can be found without ambiguity.

#### *3.2.1.2 Necessity to fit multiple populations*

Even if the population $P_1$ is not abundant, it is necessary to fit it separately from the main population $P_2$ to avoid a hot bias on the determination of the temperature of $P_2$. For comparison, we studied the case where the current curve is fitted using only one population, as shown in Figure 1a. The results are compared in Figure 11. Forcing only one electron population ($P_2$, dark blue) overestimates the temperature of the dominant population ($P_2$, light blue) by ~0.01 eV (~120 K). In addition, the total electron density increases of ~10% and is no longer consistent with the density measured by Edberg et al. (2013).

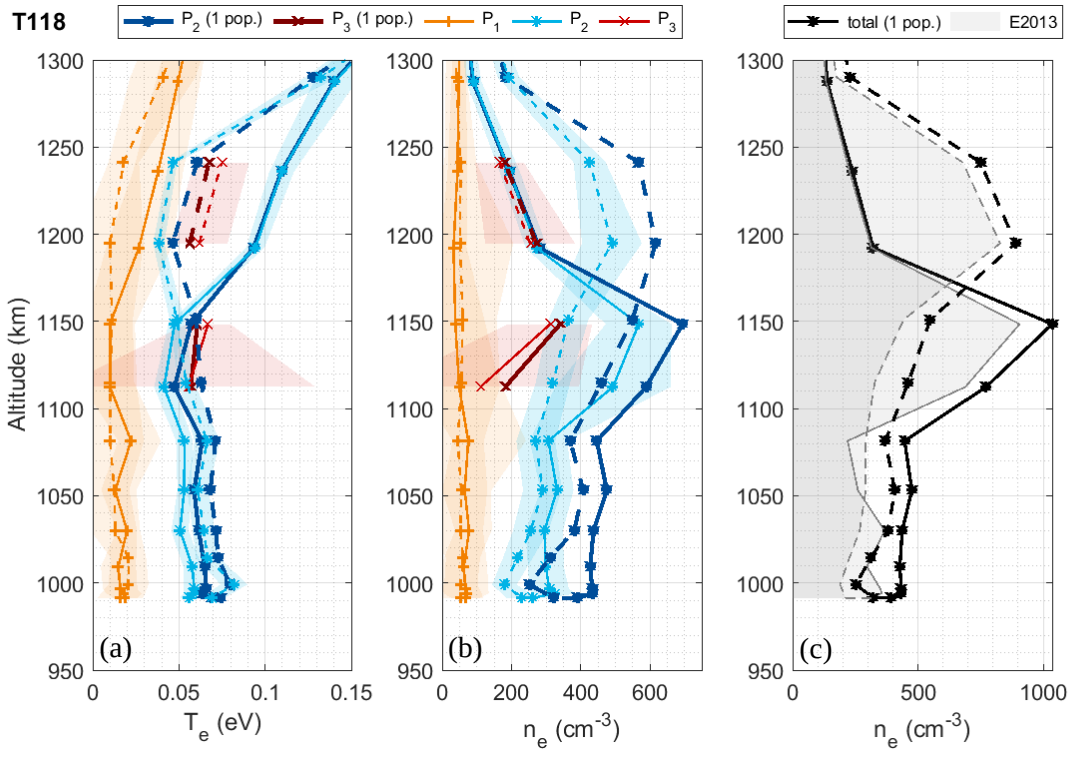


**Figure 11.** Same as Figure 10, superimposed to the $T_e$ and $n_e$ profiles obtained with only one population to fit $P_1$ and $P_2$ when their potentials are close enough (i.e. below 1200 km for inbound, and below 1300 km for outbound).

384

385 *3.2.1.3 Discussion on the origin of $P_1$ and $P_2$*

386 On the nightside far from the terminator, ionization is not governed by solar photons, but by
387 energetic particles coming from the magnetosphere (Ågren et al., 2007; Cravens et al., 2008). We
388 therefore assume that the dominant electron population ($P_2$) is the bulk of thermalized electrons
389 initially formed by energetic magnetospheric particles.

390 The other population present at all altitudes, $P_1$, is certainly due to electrons emitted by the nearby
391 probe boom, from collisions with energetic particles. Such electrons are created on the nearby
392 surfaces, they have low energy and are easily caught back. Therefore, $P_1$ corresponds to the
393 population with the lower potential $U_p$.

394 $P_3$ is discussed in the following sections, as it is observed in higher quantities in groups G2 and
395 G3.

396

397 *3.2.2 Nightside close to the terminator (group G2)*

398 *3.2.2.1 Typical altitude profiles*

399 Flybys on the nightside close to the terminator (~90° < SZA ~< 140°) show the presence of the
400 third population at all altitudes (see Figure 12).

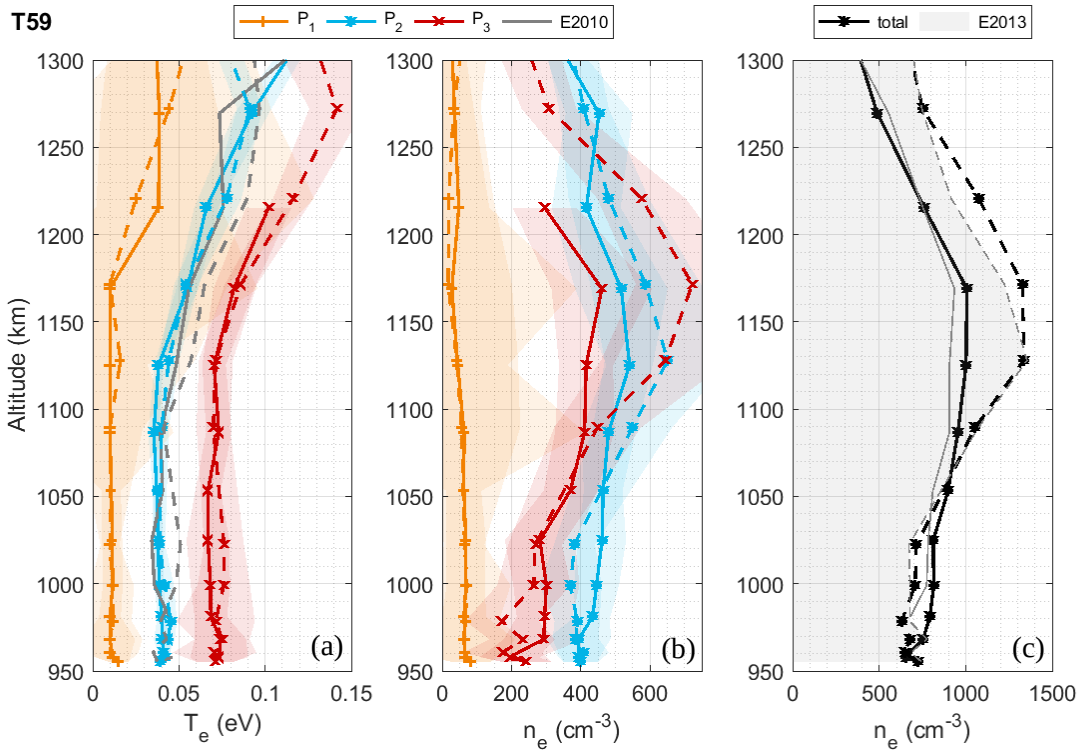


401

402 **Figure 12.** Same as Figure 10, in the case of T59, an example of a G2 group flyby (nightside close to the
403 terminator).

The total electron density is globally higher than for G1 flybys (far nightside), which is expected because of the closer influence of photoionization on dayside (Ågren et al., 2009). The temperatures observed for the three populations are similar to the ones of G1 flybys: $P_1$ below 20 meV (~230 K, orange), $P_2$ generally between 30 and 50 meV (350-580 K, blue) and $P_3$ at 60-80 meV (700-930 K, red).

#### *3.2.2.2 Necessity to fit multiple populations*

The addition of the third population ($P_3$) does not disturb the fitting of the two first populations. Besides, it is necessary to include it to obtain a total electron density similar to Edberg et al. (2013). This effect is showed in Figure 13. It compares the results obtained in Figure 12 with results of a fit that does not include the population $P_3$, as plotted in Figure 2 (a). Then, the temperatures obtained for $P_1$ and $P_2$ are almost unchanged, but the total electron density decreases of 25%.

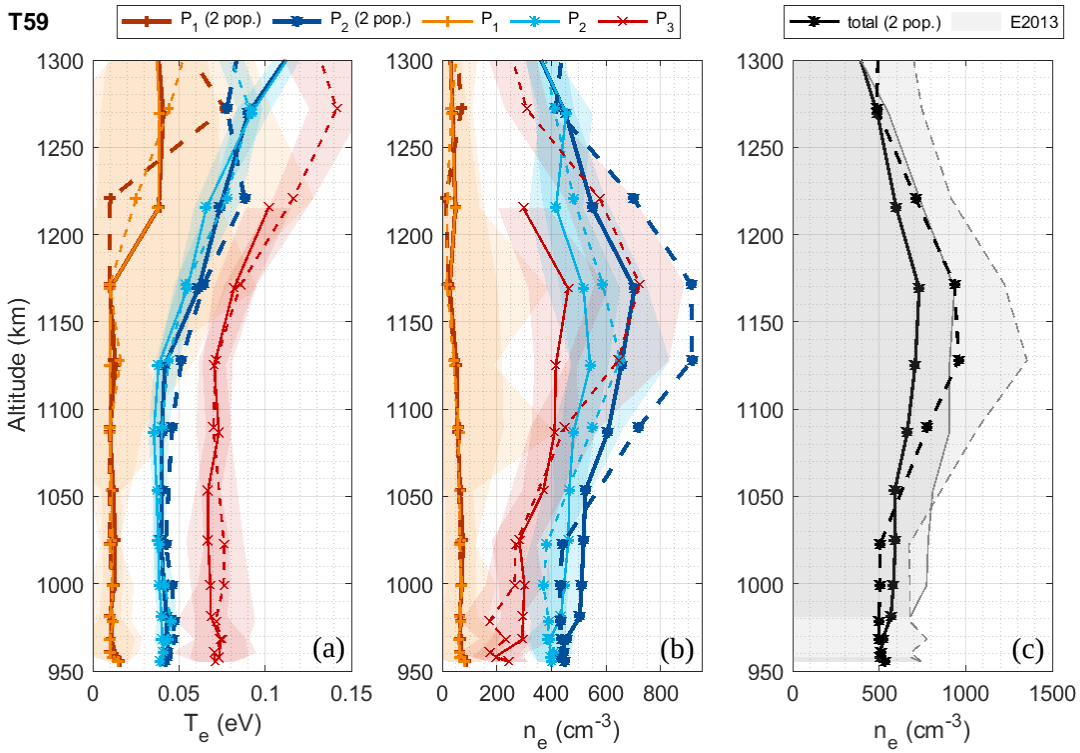


**Figure 13.** Same as Figure 12, superimposed to the $T_e$ and $n_e$ profiles obtained for $P_1$ and $P_2$ when $P_3$ is not fitted.

#### *3.2.2.3 Discussion on the origin of $P_3$*

The fact that $P_3$ is observed on dayside (G3) but not on the far nightside (G1), suggests that it is due to the efficient photo-ionization processes happening on the dayside, whose influence is

extended by transport as far as the nightside close to the terminator. However, one should also consider a possible effect of the active ion chemistry happening in these regions on the characteristics of the electron population $P_3$. In particular, the ionosphere environment on the nightside close to the terminator is enabling the growth of large ions, which is otherwise disrupted under direct extreme UV fluxes (Shebanits et al., 2017b, 2017a; Wellbrock et al., 2019).

### *3.2.3 Dayside (group G3)*

#### *3.2.3.1 Typical altitude profiles*

On dayside, a new population ($P_4$) appears in the LP sweep data at a potential $U_P$ higher than for $P_1$, $P_2$ and $P_3$. Its temperature is generally higher than for the other populations, up to 0.1 eV (~1160 K, green). This population appears only at altitudes below ~1200-1150 km and its density increase with decreasing altitude. In some cases (T17, T20, T85, T88, T104, T108), it even becomes the dominant population below 1050-1000 km, as shown in Figure 14. Contrary to the constant profiles on the nightside, the temperatures of all the populations decrease slightly with altitude, of ~0.03 eV (~350 K) in 200 km.

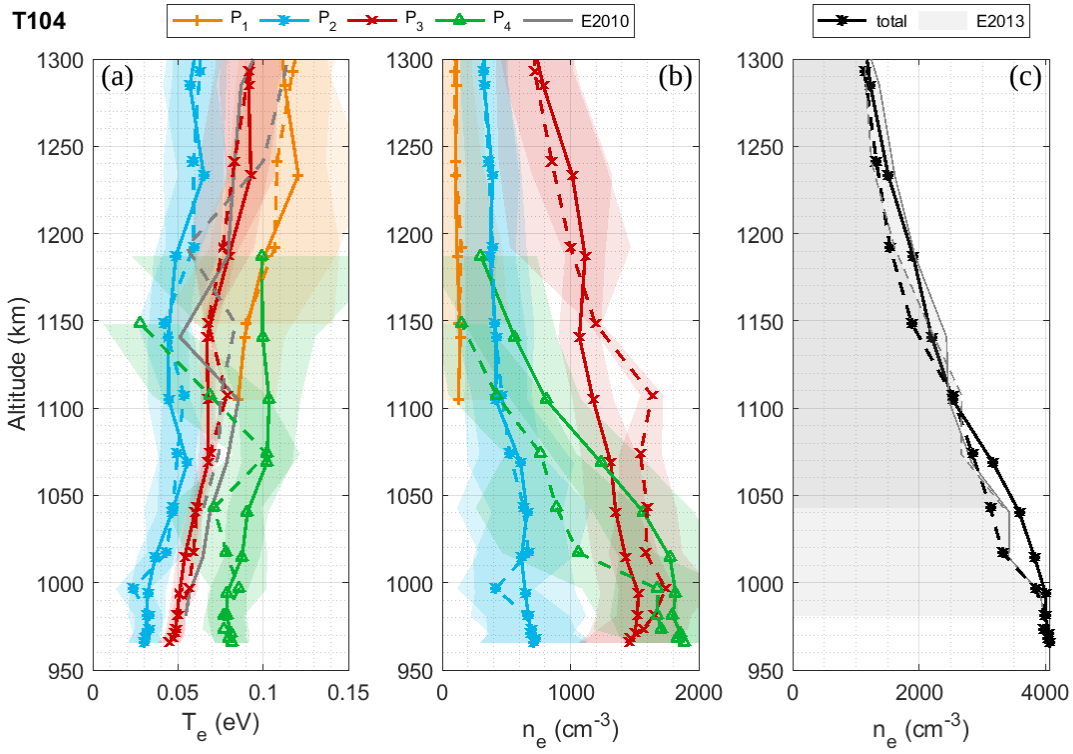


**Figure 14.** Same as Figure 10, in the case of a T104, an example of a G3 group flyby (dayside).

#### *3.2.3.2 Necessity to fit $P_4$ and fusion of $P_2$ and $P_3$*

The electron population $P_4$ is often non-negligible and should always be taken into account when present. An example of the results obtained if $P_4$ is not fitted is given in Supporting Information Figure S7. The results are similar to Section 3.2.2.2: the ($U_p$, $n_e$, $T_e$) results for the other populations are not impacted, but the total electron density is underestimated by up to 30%.

In some cases, the fitting of $P_2$ and $P_3$ can be ambiguous, especially at lower altitudes. The use of two distinct populations is required to obtain a very good fitting (examples of sweeps are given in Supporting Information Figure S8) and is consistent across all altitudes (see Figure 7 for T104). Nevertheless, the fusion of $P_2$ and $P_3$ at lower altitudes in G3 flybys happens smoothly: at one point, fitting with two or three populations gives globally the same results: $P_2$ becomes negligible compared to $P_3$. An example of the $n_e$ and $T_e$ profiles obtained when $P_2$ and $P_3$ are fitted by only one population at lower altitude is given in Supporting Information Figure S9. The total electron density stays globally the same, the temperature of the main population is not impacted and the population $P_4$ generally stays in the range of its large error bars.

#### *3.2.3.3 Discussion on the origin of $P_1$ and $P_4$*

Similarly to the nightside, $P_1$ electrons on the dayside are certainly emitted by the probe boom. However, on dayside, the photoemission is also possible. In this case, the emitted electrons observed are hotter than on nightside.

The population $P_4$ is only detected on dayside. We argue here that it is not an instrumental effect but rather due to dusty plasma:

- Energetic photons and particles can detach electrons from the surface of the spacecraft. Nevertheless, in the ionosphere the electrons are cold enough to prevent these spacecraft electrons to reach the Langmuir probe (Wang et al., 2015). Indeed, the Debye length in the ionosphere is always below 10.5 cm, far lower than the distance between the spacecraft and the Langmuir Probe (which is on a 1.5 m boom).

- The spacecraft motion cannot explain the presence of several electron populations. With energies from 0.02 to 0.08 eV in the ionosphere, the electrons of the various populations have a thermal velocity of 85 to 170 km/s, much larger than the spacecraft velocity (~6 km/s). Therefore, there should be no difference in the electron collection from all around the probe.

- The perturbation of the collected current by organic deposit on the surface of the probe is not likely. In theory, the complex organic chemistry happening in the ionosphere could possibly lead to the formation of a deposit on the surface of the probe during the 10-15 minutes long ionosphere pass. Such a film coating, depending on the surface coverage and dielectric properties, would induce the detection of several electron components in the sweeps. However, no indication of this has been observed when comparing the sweeps ‘down’ and ‘up’ (see Section 2.1, Appendix A and Supporting Information Figure S1). Additionally, the probe is cleaned between two flybys (see Section 2.1), and observations during the inbound and the outbound are very similar (in the case of flybys with inbound and outbound at similar SZA).

- $P_4$ is possibly due to a dusty plasma effect. Indeed, it is not predicted by current ionospheric models that do not include the effect of the charged dust grains or aerosols on the electron

populations. The fourth electron population is only detected in the regions where dusty plasma has been previously measured (Shebanits et al., 2016), this suggests the charged dust grains to be the cause, either as a source or a disruption of the ambient electrons. This possibility is investigated in paper II.

## 4 Conclusions

The re-analysis of the Langmuir probe data in Titan's ionosphere brought new insights on the behavior of the electrons in this environment.

The detailed analysis of the data revealed the presence of several electron populations, at different potentials, and with different electron densities and temperatures. We have shown that the second derivative of the electron current collected by the Langmuir probe during a voltage sweep is a useful tool to detected the presence of several electron populations, especially as it is linked to the electron energy distribution function (EEDF) (Druyvesteyn, 1930). With the evolution of the second derivative of the current with altitude we observed the evolution of the electron populations with altitude in three different conditions: far nightside (T118), nightside close to the terminator (T59) and dayside (T104).

Two populations (with the lower potentials) are present in nearly all conditions. The third population is not observed on the far nightside, and the fourth is detected on dayside below 1200-1150 km. We have investigated the fitting of the electron current curve with 2 to 4 populations with a systematic approach on all flybys that validated the presence of 2, 3 or 4 populations only depending on the altitude and the solar illumination. A rigorous testing on the number of fitted populations shows that the fitting of all the detected populations (i.e. the whole electron distribution) is necessary to obtain a correct fit and retrieve the total electron density previously deduced from different methods (Ågren et al., 2009; Edberg et al., 2013; Garnier et al., 2009).

We suggested possible origins for the four populations:

- $P_1$ electrons, with the lowest potential and a low density, are emitted by the probe boom;
- a likely cause for the $P_2$ electrons, found even on the far nightside, is the thermalization of magnetospheric electrons;
- $P_3$ electrons, not present on the far nightside, are likely to be related to photo-ionization;
- and $P_4$ electrons, observed at lower altitudes on dayside, are plausibly linked to dusty plasma effects.

These four populations are studied in more details in paper II that performs a complete investigation on all the Cassini Langmuir probe dataset in the ionosphere of Titan.

## Acknowledgments and Data

The Swedish National Space Board (SNSB) supports the RPWS/LP instrument on board Cassini. A.C. acknowledges ENS Paris-Saclay Doctoral Program. A.C. is grateful to Anders Eriksson, Jean-Pierre Lebreton, Erik Vigren and Ronan Modolo for fruitful discussions on this project. O.S. acknowledges funding by the Royal Society grant RP\EA\180014. N.J.T.E. was funded by the Swedish National Space Board under contract 135/13 and by the Swedish Research Council under contract 621-2013-4191. N.C. acknowledges the financial support of the European Research Council (ERC Starting Grant PRIMCHEM, Grant agreement no. 636829).

All Cassini RPWS data are archived in the Planetary Data System (PDS) Planetary Plasma Interaction (PPI) node at https://pds-ppi.igpp.ucla.edu on a pre-arranged schedule.


## Appendix A.

We investigated the reproducibility of the measurements with the two voltage sweeps (named 'down' and 'up'), and the double measurements at each voltage step (resp. 'down1'-'down2' and 'up1'-'up2'). Figure A1 shows the comparison.

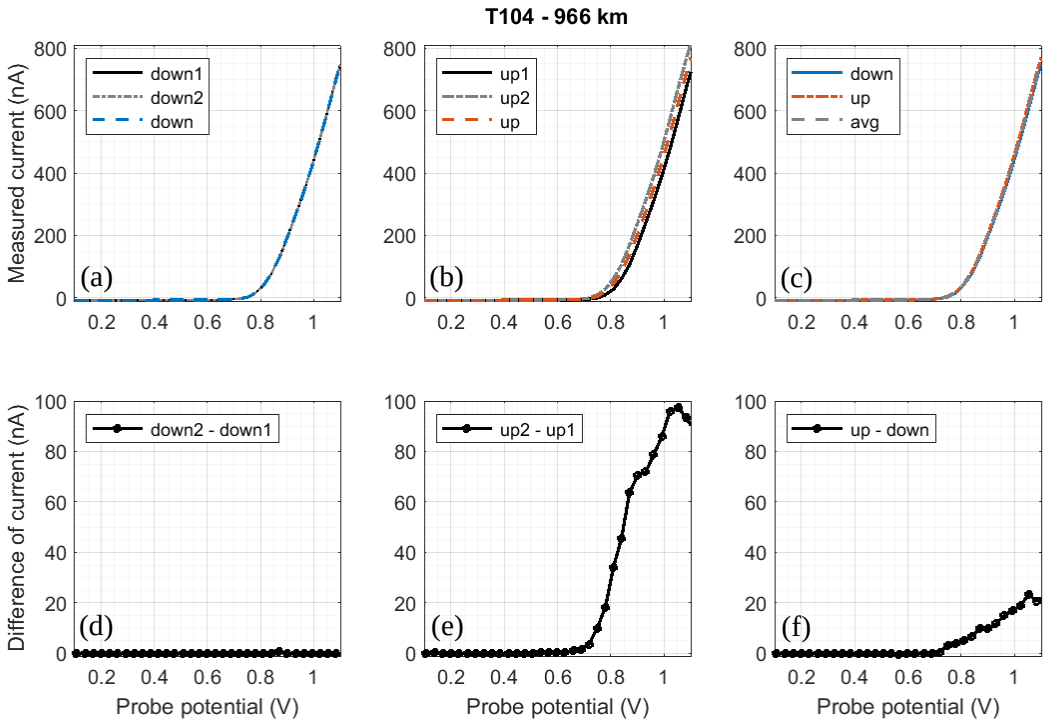


**Figure A1.** Raw data of the acquisition of a LP sweep. Left: data from the decreasing phase: (a) first point acquired ('down1'), second point acquired ('down2'), the average of both ('down') and (b) their difference ('down2 – down1'). Middle: the same for the increasing phase, respectively (b) and (e). Right: (c) the average for the decreasing and increasing phases, the average of both ('avg') and (f) their difference ('up – down'). From a measurement at ~966 km, during the Titan flyby T104.

The two data points taken at a same voltage step during the decreasing voltage phase ('down1' and 'down2') are always very close to each other: the current stabilizes quickly at after each voltage step. However, during the increasing voltage phase ('up1' and 'up2'), the current continues to increase between the two measurements: the current takes longer to stabilize, especially in the strongly varying exponential parts of the sweep.

Figure A2 shows the variations 'down2 – down1', 'up2 – up1' and 'up – down' with altitude for 26 flybys on dayside and 8 flybys on nightside far from the terminator. In each case, we selected the largest difference of current and the maximum of the averaged current in the voltage range [Up1 – 0.7, Up1 + 0.3], Up1 being the plasma potential of the first population (it is located at the beginning of the increase of the current and is more precisely defined below). Figure A2 shows their ratio (difference / average) as a function of altitude. In all cases, the difference 'down2 – down1' (blue triangles) is very small, as opposed to 'up2 – up1' (orange squares) that ranges from 9 to 23%. The difference 'up – down' (black stars) is often negative, and inferior to 10% in absolute values.

The difference between 'up1' and 'up2' shows that the collected current is not stabilized, and increases between the acquisition of the two points on a same voltage step. On nightside flybys (Figure A2b), the difference 'up2 – up1' varies smoothly with altitude, while on dayside flybys (Figure A2a) a sudden change in the difference is always observed between 1100 and 1200 km.

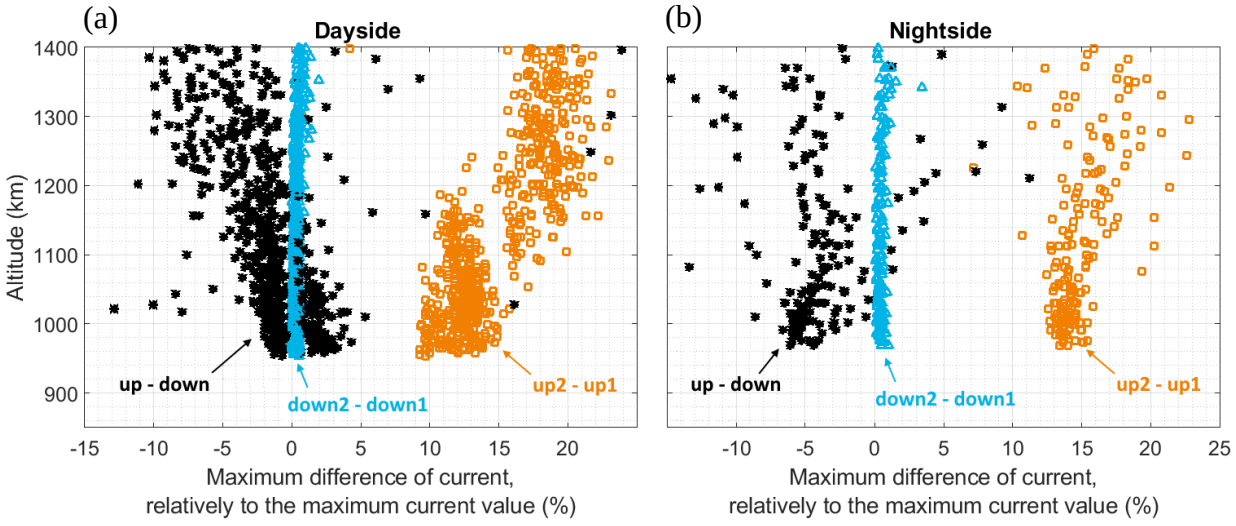


**Figure A2.** Maximum differences of the current ('down2 – down1', 'up2 – up1' and 'up – down') in the voltage range [Up1 – 0.7, Up1 + 0.3] as a function of altitude. The maximum differences are divided by the maximum of the averaged current to facilitate the comparison at different altitudes. (a) Flybys on dayside. (b) Flybys on nightside, far from the terminator.

## Appendix B. Algorith to fit the voltage sweeps with several populations

To constrain the fitting of voltage sweeps in the case of several electron populations, the following procedure is used:

1/ detection of the increase of the current (generally above 0.8 nA) and of the saturated part ($U_{lim}$);

2/ search for peaks in the second derivative of the current ($d^2I/dU^2$) in the voltage interval defined in 1/;

3/ selection of the part of the voltage sweep ($I_1$) with a voltage inferior to the potential corresponding to the minimum of $d^2I/dU^2$ between the two first peaks (or < $U_{lim}$ if there is only 1 population);

4/ fit of the current curve for the first population with Equations (2) and (5) in the reduced voltage interval $I_1$;

If there is more than 1 population:

5/ selection of the part of the curve ($I_2$) with a voltage inferior to the potential corresponding to the minimum of $d^2I/dU^2$ between peak 2 and peak 3 (or < $U_{lim}$ if there are only 2 populations);

6/ fit of populations 1 and 2 with two set of Equations (2) and (5) in the reduced voltage interval $I_2$, the initial parameters for the fit of the first population being given by 4/;

If there are more than 2 populations:

7/ selection of the part of the curve ($I_3$) with a voltage inferior to the potential corresponding to the minimum of $d^2I/dU^2$ between peak 3 and peak 4 (or < $U_{lim}$ if there are only 3 populations);

8/ fit of populations 2 and 3 with two set of Equations (2) and (5) in the reduced voltage interval $I_3$, the initial parameters for the fit of population 2 being given by 6/. The contribution of population 1 is beforehand removed, based on the fit results in 6/;

If there are more than 3 populations:

9/ selection of the part of the curve ($I_4$) with a voltage inferior to $U_{lim}$;

10/ fit of populations 3 and 4 with two set of Equations (2) and (5) in the reduced voltage interval $I_4$, the initial parameters for the fit of population 3 being given by 8/. The contributions of populations 1 and 2 are beforehand removed, based on the fit results in respectively 6/ and 8/;

## Appendix C. Confidence intervals for fit results

The parameters fitted are not directly ($U_P$, $n_e$, $T_e$), but ($U_P, I_0, \beta = 1/T_e$), with $T_e$ the electron temperature in electron volt. The confidence intervals for the last three parameters are obtained at

95%. The standard deviation is then easily deduced for $U_P$ and $T_e$. Concerning $n_e$, the standard deviation ($\sigma_{n_e}$) is obtained by the following equation, derived from Equation (3) applied to electrons:

$$\sigma_{n_e} = \left(\frac{\sqrt{2\pi m_e}}{A_{LP} e^{3/2}}\right) \times \left(\sigma_{I_0} . \sqrt{\beta} + I_0 . \frac{\sigma_\beta}{2\sqrt{\beta}}\right) \quad \text{(C-1)}$$

with $I_0$ and $\beta$ obtained by the fit, and $\sigma_{I_0}$ and $\sigma_\beta$ their standard deviations.

## Appendix D. Equation linking the EEDF to the second derivative of the current (Druyvesteyn method)

The equation for the electron velocity distribution as function of the second derivative of the electron current is given by the equation (3) in Druyvesteyn (1930):

$$\mathcal{V}\,(\Delta U) = \frac{4\, m_e}{A_{LP}\, e^2} \cdot \Delta U \cdot \frac{d^2 I_e}{d\Delta U^2} \qquad [(m.s^{-1})^{-1}.m^{-3}] \quad \text{(D-1)}$$

Electrons with a speed between $v$ and $v + dv$ have energies between $E$ and $E + dE$, therefore:

$$\mathcal{V}(v).dv = EEDF(E).dE \quad \text{(D-2)}$$

The derivative of the speed with respect to energy is given by:

$$E = \frac{1}{2} m_e v^2 \quad => \quad \frac{dv}{dE} = (2 m_e E)^{-\frac{1}{2}} \quad \text{(D-3)}$$

Therefore, we obtain the EEDF by dividing the electron speed distribution by $\sqrt{2m_e E}$, with $E(\Delta U) = -e\,.\Delta U$:

$$EEDF_{Dr}\,(\Delta U) = \frac{2\sqrt{2}}{A\, e^2} \sqrt{\frac{m\,.(-\Delta U)}{e}}\, \frac{d^2 i}{d\Delta U^2} \qquad [J^{-1}.m^{-3}]$$
$$with\ n_e = \int_0^{+\infty} EEDF_{Dr}\big(E(\Delta U)\big)\,.dE \quad \text{(D-4)}$$

630 **References**

631

632 Ågren, K., Wahlund, J. E., Modolo, R., Lummerzheim, D., Galand, M., Müller-Wodarg, I., et al.
633 (2007). On magnetospheric electron impact ionisation and dynamics in Titan's ram-side and
634 polar ionosphere - a Cassini case study. *Annales Geophysicae*, *25*(11), 2359–2369.
635 https://doi.org/10.5194/angeo-25-2359-2007

636 Ågren, K., Wahlund, J.-E., Garnier, P., Modolo, R., Cui, J., Galand, M., & Müller-Wodarg, I.
637 (2009). On the ionospheric structure of Titan. *Planetary and Space Science*, *57*(14–15),
638 1821–1827. https://doi.org/10.1016/J.PSS.2009.04.012

639 Bettinger, R. T., & Walker, E. H. (1965). Relationship for Plasma Sheaths about Langmuir Probes.
640 *The Physics of Fluids*, *748*(8), 748–751. https://doi.org/10.1063/1.1761293

641 Chatain, A., Wahlund, J. -E., Shebanits, O., Hadid, L. Z., Eriksson, A. I., Morooka, M. W., et al.
642 (n.d.). Re-analysis of the Cassini RPWS/LP data in Titan's ionosphere. Part II: statistics on
643 57 flybys. *Journal of Geophysical Research: Space Physics*, *submitted*.

644 Coates, A. J., Crary, F. J., Lewis, G. R., Young, D. T., Waite, J. J. H., & Sittler, J. E. C. (2007).
645 Discovery of heavy negative ions in Titan's ionosphere. *Geophysical Research Letters*, *34*,
646 L22103. https://doi.org/10.1029/2007GL030978

647 Cravens, T. E., Robertson, I. P., Ledvina, S. A., Mitchell, D., Krimigis, S. M., & Waite, J. H.
648 (2008). Energetic ion precipitation at Titan. *Geophysical Research Letters*, *35*(3), L03103.
649 https://doi.org/10.1029/2007GL032451

650 Cravens, T. E., Robertson, I. P., Waite, J. H., Yelle, R. V., Vuitton, V., Coates, A. J., et al. (2009).
651 Model-data comparisons for Titan's nightside ionosphere. *Icarus*, *199*(1), 174–188.
652 https://doi.org/10.1016/j.icarus.2008.09.005

653 Cui, J., Galand, M., Yelle, R. V., Vuitton, V., Wahlund, J. E., Lawas, P. P., et al. (2009). Diurnal
654 variations of Titan's ionosphere. *Journal of Geophysical Research: Space Physics*, *114*,
655 A06310. https://doi.org/10.1029/2009JA014228

656 Druyvesteyn, M. J. (1930). Der niedervoltbogen. *Zeitschrift Für Physik*, *64*(11–12), 781–798.

657 Edberg, N. J. T., Wahlund, J. E., Ågren, K., Morooka, M. W., Modolo, R., Bertucci, C., &
658 Dougherty, M. K. (2010). Electron density and temperature measurements in the cold plasma
659 environment of Titan: Implications for atmospheric escape. *Geophysical Research Letters*,
660 *37*, L20105. https://doi.org/10.1029/2010GL044544

661 Edberg, N. J. T., Andrews, D. J., Shebanits, O., Ågren, K., Wahlund, J. E., Opgenoorth, H. J., et
662 al. (2013). Solar cycle modulation of Titan's ionosphere. *Journal of Geophysical Research:*
663 *Space Physics*, *118*(8), 5255–5264. https://doi.org/10.1002/jgra.50463

664 Fahleson, U., Fälthammar, C.-G., & Pedersen, A. (1974). Ionospheric temperature and density
665 measurements by means of spherical double probes. *Planetary and Space Science*, *22*(1), 41–
666 66. https://doi.org/10.1016/0032-0633(74)90122-6

667 Farrell, W. M., Kurth, W. S., Gurnett, D. A., Johnson, R. E., Kaiser, M. L., Wahlund, J.-E., &
668 Waite, J. H. (2009). Electron density dropout near Enceladus in the context of water-vapor
669 and water-ice. *Geophysical Research Letters*, *36*(10), L10203.

https://doi.org/10.1029/2008GL037108

Galand, M., Coates, A. J., Cravens, T. E., & Wahlund, J.-E. (2014). Titan's Ionosphere. In *Titan* (pp. 296–361). Cambridge, UK: Cambridge University Press.

Garnier, P., Wahlund, J., Rosenqvist, L., Modolo, R., Agren, K., Canu, P., et al. (2009). Titan's ionosphere in the magnetosheath: Cassini RPWS results during the T32 flyby. *Annales Geophysicae*, *27*, 4257–4272.

Gurnett, D. A., Kurth, W. S., Kirchner, D. L., Hospodarsky, G. B., Averkamp, T. F., Zarka, P., et al. (2004). The Cassini Radio and Plasma Wave Investigation. In *The Cassini-Huygens Mission* (pp. 395–463). Springer Netherlands. https://doi.org/10.1007/978-1-4020-2774-1_6

Lieberman, M. A., & Lichtenberg, A. J. (2005). *Principles of Plasma Discharges and Materials Processing: Second Edition*. *Principles of Plasma Discharges and Materials Processing: Second Edition*. https://doi.org/10.1002/0471724254

Mott-Smith, H. M., & Langmuir, I. (1926). The theory of collectors in gaseous discharges. *Physical Review*, *28*(4), 727–763. https://doi.org/10.1103/PhysRev.28.727

Mukundan, V., & Bhardwaj, A. (2018). Dayside ionosphere of Titan: Impact on calculated plasma densities due to variations in the model parameters. *Icarus*, *299*, 222–239. https://doi.org/10.1016/j.icarus.2017.07.022

Richard, M. S., Cravens, T. E., Robertson, I. P., Waite, J. H., Wahlund, J.-E., Crary, F. J., & Coates, A. J. (2011). Energetics of Titan's ionosphere: Model comparisons with Cassini data. *Journal of Geophysical Research: Space Physics*, *116*, A09310. https://doi.org/10.1029/2011JA016603

Shebanits, O., Wahlund, J. E., Mandt, K., Ågren, K., Edberg, N. J. T., & Waite, J. H. (2013). Negative ion densities in the ionosphere of Titan-Cassini RPWS/LP results. *Planetary and Space Science*, *84*, 153–162. https://doi.org/10.1016/j.pss.2013.05.021

Shebanits, O., Wahlund, J.-E., Edberg, N. J. T., Crary, F. J., Wellbrock, A., Andrews, D. J., et al. (2016). Ion and aerosol precursor densities in Titan's ionosphere: A multi-instrument case study. *Journal of Geophysical Research: Space Physics*, *121*(10), 10,075-10,090. https://doi.org/10.1002/2016JA022980

Shebanits, O., Vigren, E., Wahlund, J.-E., Edberg, N. J. T., Cui, J., Mandt, K. E., & Waite, J. H. (2017a). Photoionization Modeling of Titan's Dayside Ionosphere. *The Astrophysical Journal*, *850*(2), L26. https://doi.org/10.3847/2041-8213/aa998d

Shebanits, O., Vigren, E., Wahlund, J. E., Holmberg, M. K. G., Morooka, M., Edberg, N. J. T., et al. (2017b). Titan's ionosphere: A survey of solar EUV influences. *Journal of Geophysical Research: Space Physics*, *122*(7), 7491–7503. https://doi.org/10.1002/2017JA023987

Shukla, P. K., & Mamun, A. A. (2015). *Introduction to dusty plasma physics*. *Introduction to Dusty Plasma Physics*. CRC Press. https://doi.org/10.1088/0741-3335/44/3/701

Vigren, E., Galand, M., Yelle, R. V., Cui, J., Wahlund, J. E., Ågren, K., et al. (2013). On the thermal electron balance in Titan's sunlit upper atmosphere. *Icarus*, *223*(1), 234–251. https://doi.org/10.1016/j.icarus.2012.12.010

Vigren, E., Galand, M., Wellbrock, A., Coates, A. J., Cui, J., Edberg, N. J. T., et al. (2016).

Suprathermal electrons in Titan's sunlit ionosphere: model-observation comparisons. *The Astrophysical Journal*, *826*(2), 131. https://doi.org/10.3847/0004-637x/826/2/131

Vuitton, V., Yelle, R. V., Klippenstein, S. J., Hörst, S. M., & Lavvas, P. (2019). Simulating the density of organic species in the atmosphere of Titan with a coupled ion-neutral photochemical model. *Icarus*, *324*, 120–197. https://doi.org/10.1016/j.icarus.2018.06.013

Wahlström, M. K., Johansson, E., Veszelei, E., Bennich, P., Olsson, M., & Hogmark, S. (1992). Improved Langmuir probe surface coatings for the Cassini satellite. *Thin Solid Films*, *220*, 315–320. https://doi.org/10.1016/0040-6090(92)90591-X

Wahlund, J. E., Boström, R., Gustafsson, G., Gurnett, D. A., Kurth, W. S., Pedersen, A., et al. (2005). Cassini measurements of cold plasma in the ionosphere of Titan. *Science*, *308*(5724), 986–989. https://doi.org/10.1126/science.1109807

Wahlund, J. E., André, M., Eriksson, A. I. E., Lundberg, M., Morooka, M. W., Shafiq, M., et al. (2009). Detection of dusty plasma near the E-ring of Saturn. *Planetary and Space Science*, *57*(14–15), 1795–1806. https://doi.org/10.1016/j.pss.2009.03.011

Waite, J. H., Niemann, H., Yelle, R. V., Kasprzak, W. T., Cravens, T. E., Luhmann, J. G., et al. (2005). Ion Neutral Mass Spectrometer results from the first flyby of Titan. *Science*, *308*(5724), 982–986. https://doi.org/10.1126/science.1110652

Waite, J. H., Young, D. T., Cravens, T. E., Coates, A. J., Crary, F. J., Magee, B., & Westlake, J. (2007). Planetary science: The process of tholin formation in Titan's upper atmosphere. *Science*, *316*(5826), 870–875. https://doi.org/10.1126/science.1139727

Wang, X., Hsu, H. W., & Horányi, M. (2015). Identification of when a Langmuir probe is in the sheath of a spacecraft: The effects of secondary electron emission from the probe. *Journal of Geophysical Research: Space Physics*, *120*, 2428–2437. https://doi.org/10.1002/2014JA020624

Wellbrock, A., Coates, A. J., Jones, G. H., Vuitton, V., Lavvas, P., Desai, R. T., & Waite, J. H. (2019). Heavy negative ion growth in Titan's polar winter. *Monthly Notices of the Royal Astronomical Society*, *490*(2), 2254–2261. https://doi.org/10.1093/mnras/stz2655

Whipple, E. C. J. (1965). The equilibrium electric potential of a body in the upper atmosphere and in the interplanetary space. *PhD Thesis, George Washington University*.